Black Gold Plasmon Response of a Raspberry Shell Grown on Lithium Niobate Nonlinear Nanoparticles

Kévin Bredillet, Zacharie Behel, Rachael Taitt, Mathias Urbain, Jaona Harifidy Randrianalisoa, Sandrine Beauquis, Yannick Mugnier, Pierre-François Brevet, Ronan Le Dantec, Yann Chevolot, et al.

Black Gold Plasmon Response of a Raspberry Shell grown on Lithium Niobate Nonlinear Nanoparticles

*Kévin Bredillet[1], Zacharie Behel[2], Rachael Taitt[3], Mathias Urbain[1], Jaona Harifidy Randrianalisoa[4], Sandrine Beauquis[1], Yannick Mugnier[1], Pierre-François Brevet[2], Ronan Le Dantec[1], Yann Chevolot[5], Virginie Monnier[3]**

[1] Université Savoie Mont Blanc, SYMME, F-74000 Annecy, France.

[2] Université de Lyon, Université Claude Bernard Lyon 1, UMR CNRS 5306, Institut Lumière Matière, F-69622 Villeurbanne, France.

[3] Univ Lyon, Ecole Centrale de Lyon, CNRS, INSA Lyon, Université Claude Bernard Lyon 1, CPE Lyon, CNRS, INL, UMR5270, 69130 Ecully, France.

[4] Institut de Thermique, Mécanique, Matériaux (ITheMM EA 7548), Université de Reims Champagne-Ardenne, Campus du Moulin de la Housse, F-51687, Reims, France.

[5] Univ Lyon, CNRS, INSA Lyon, Ecole Centrale de Lyon, Université Claude Bernard Lyon 1, CPE Lyon, INL, UMR5270, 69130 Ecully, France.

KEYWORDS. Plasmonic gold shell, lithium niobate nanoparticles, modelling, hyperpolarizability, SHS spectroscopy.

ABSTRACT. Lithium niobate nanoparticles coated with a raspberry-like gold shell are synthesized. The strong plasmon resonance coupling between gold nanoparticles in raspberry nanostructures is expected to modify the surface and cavity optical fields and thus significantly alter the second harmonic signal generated by the non-centrosymmetric crystalline core of lithium niobate. Plasmonic properties of the core-shell nanoparticles are first modelled using the Discrete-Dipole Approximation (DDA) method. The influence of the size and filling fraction of gold nanoparticles on the extinction cross-section is correlated with the experimental responses. Comparison at 800 nm of the first hyperpolarizability of individual gold nanoparticles, bare lithium niobate cores and hybrid nanostructures demonstrates no enhancement. It reveals instead an octupolar response in the polarization-resolved data consistent with a dominant surface contribution of the raspberry-like gold shell. The wavelength-dependent second harmonic emission of the hybrid nanostructures is finally determined in the 700-1300 nm excitation range and a continuous increase that reaches a factor up to 20 is only evidenced at the longest excitation wavelength of 1300 nm.

1. INTRODUCTION

Gold nano-raspberries with a rough surface are composed of a core material decorated with closely-packed spherical gold nanoparticles (NPs). Due to the short distance between gold NPs, their surface plasmon resonance can be coupled, leading to the broadening of their absorbance in the near-infrared region,[1] a large scattering cross-section and enhanced surface and cavity electromagnetic fields.[2] Specific functionalities are thus achieved with applications as Surface-Enhanced Scattering (SERS) nanosensors[3] and photothermal therapeutic agents.[4] These rough gold nanostructures are typically grown as surrounding shells onto a variety of core materials

including polymer,[5] silica,[6] organic framework,[3] metal[7] or magnetite.[8] Recently, hollow raspberry-like gold NPs were also produced.[9,10]

Here, lithium niobate ($LiNbO_3$, LN) was selected as the core material to grow a raspberry-like gold shell. Due to its non-centrosymmetric crystalline structure, LN is a mixed-metal oxide exhibiting piezoelectricity, electro-optics and second-order nonlinear optical properties at the nanoscale for both multimodal imaging and the photo-triggered release of chemotherapeutics.[11–13] Combining the intrinsic nonlinear optical properties of non-centrosymmetric oxide materials with plasmonic resonances is an effective way to enhance several nonlinear processes as already demonstrated for mesoporous LN microspheres[14], for LN bulk crystals combined to various gold nanostructures[15,16] and for another dielectric core composed of barium titanate ($BaTiO_3$).[17–19] Note that in the bulk form, hybrid plasmonic waveguides are able to produce giant second harmonic signals thanks to the influence of plasmonic resonances onto the confined modes.[20,21] The encapsulation of LN NPs into a raspberry-like gold nanoshell by a wet chemistry approach has several noticeable advantages. First, it avoids the difficulties related to the nanofabrication of precisely positioned nanostructures and provides a scalable elaboration route.[14] Second, the rough gold surface offers a high density of localized 'hot spots' or 'disordered nanoantennas' which may provide an increased SERS effect,[22] a better far-field coupling with long-lived plasmonic modes,[23] a tunable plasmon band over a large range of wavelengths and high absorption cross-sections. This core-shell nano-raspberry structure is thus expected to strongly influence the nonlinear optical properties of LN such as its wavelength-dependent second harmonic generation (SHG), first hyperpolarizability and depolarization ratio.

In our previous works, we first synthesized and studied the influence of various densities of gold nano-seeds onto LN NPs.[24] The first hyperpolarizability was shown to slightly decrease at high

surface densities of gold nano-seeds for an almost constant depolarization ratio corresponding to the one of bare LN, thus evidencing the predominance of the core volume contribution. Gold seeds were then grown and the as-obtained raspberry-like gold nanoshells onto LN NPs were thoroughly optimized and characterized.[25] As expected, broad plasmonic responses were demonstrated from the extinction spectra.

In this paper, we focus on the study of the plasmonic and nonlinear optical properties of these hybrid lithium niobate-gold core-shell NPs. A model based on Discrete-Dipole Approximation (DDA) is first proposed to compute the plasmonic behavior of the raspberry-like gold shell according to the gold NPs size and density. After verification of the black gold plasmonic regime, the nonlinear optical properties of the optimized hybrid nanostructure are characterized. Hyper Rayleigh Scattering (HRS) experiments are performed at 800 nm to measure the first hyperpolarizability and depolarization ratio of both gold NPs, bare lithium niobate cores and hybrid nanostructures. Second Harmonic Spectroscopy (SHS) is finally used to probe any enhancement effect in the 700-1300 nm excitation range.

2. EXPERIMENTAL

2.1. Synthesis of lithium niobate-gold core-shell (LN@Au) NPs.

The whole synthesis protocol of LN@Au synthesis is detailed in Supporting Information and in previous papers.[24,25] Briefly, LN NPs with a typical diameter of 45 nm were synthesized by a non-aqueous solvothermal alkoxide process.[26,27] Addition of Branched PolyEthylenImine (BPEI) polymer in colloidal suspensions was used to coat the LN NPs and change to positive the initial negative surface charge of LN. Negatively-charged gold seeds (AuSeeds) were synthesized using the protocol reported by Duff et al.[28] AuSeeds were then attached onto LN@BPEI NPs via

electrostatic interaction, with a theoretical ratio in number of AuSeeds to LN NPs fixed at 1000:1. The resulting LN@BPEI@AuSeeds NPs were then again coated with BPEI and a layer-by-layer (LbL) process was used to grow the gold shell. In this process, chloroauric acid trihydrate ($HAuCl_4 \cdot 3H_2O$) in presence of hydroxylamine hydrochloride (NH_2OH, HCl) as a gold reducer, were added to the LN@BPEI@AuSeeds@BPEI NPs and this last step was repeated two more times. These three reduction steps were labelled R1, R2 and R3, respectively.

2.2. Modelling of Au-decorated $LiNbO_3$ optical response.

The DDA package DDSCAT 7.3.2 developed by Draine and co-workers[29] was employed to compute the linear optical responses of Au-decorated $LiNbO_3$ nanostructures in the 400-1400 nm spectral range. The LN core was modelled as a sphere with the dielectric function taken from Zelmon *et al*[30] and Au nanospheres were randomly attached over the LN core surface.[31] Their size and number covering the core were varied in order to model the different shell nanostructures resulting from the successive steps of the LbL process. The dielectric function of Au NPs was assumed to follow the Drude permittivity model while accounting for finite size effects in the bulk dielectric function of gold.[31] Both the $LiNbO_3$ core and Au NPs were then discretized in regular arrays of spaced dipoles while the water solvent of constant refractive index at 1.33 was considered as the 'host medium'. The DDSCAT code numerically solves electromagnetic wave equations for a given geometry discretized in dipoles. The dipole spacing should be chosen small enough compared to the wavelength and any structural length in the targeted geometry to ensure accurate calculations. In this study, the dipole size was fixed at 0.5 nm enabling a good compromise between computation times and accuracy (maximum deviation less than 1% with respect to experimental data of single Au nanoparticle).[31]

2.3. Hyper Rayleigh Scattering (HRS).

Two distinct but similar experimental setups were used to investigate the Second Harmonic (SH) properties of the NPs. The first one was used to perform hyperpolarizability and polarization-resolved measurements.[32] Briefly, the output of a femtosecond Ti:Sapphire laser (Coherent, Chameleon Ultra) with a pulse duration of about 180 fs and an average power of 500 mW centered at a wavelength of 800 nm was used to generate incoherent second harmonic scattered light from the sample cell. In order to control the polarization and the energy of the light impinging onto the sample, the beam was passed through a half wave plate followed by a polarizing cube. The fundamental beam was vertically polarized and gently focused using a low NA microscope objective (X16, NA = 0.32) onto the sample cell. The latter was made from fused silica and had an optical path length of 5 mm. The 400 nm second harmonic light scattered at a right angle was then analyzed with a spectrometer (Jobin Yvon, iHR 320) and a CCD camera (Andor, Andor 440) for spectral cleaning and detection. A color filter was placed before the spectrometer as well as a set of a half wave plate and a polarizing cube to select the output polarization. For the polarization-resolved experiments, a half-wave plate was rotated before the objective to control the polarization of the fundamental beam. Each measurement was statistically analyzed and averaged over typically ten seconds of acquisition times. Second Harmonic Spectroscopy (SHS) experiments were performed with another experimental set-up already described.[33] Briefly, a tunable femtosecond laser (680 to 1300 nm, Insight X3 Spectra-Physics) is used as the excitation source and focused through an achromatic lens (f = 30 mm) into a fused silica cuvette containing the nanoparticle suspension. The incident power is controlled with an achromatic half-wave plate (Thorlabs, 690-1200 nm) coupled to a vertical Glan-laser polarizer. The emitted signal is collected

perpendicularly to the incident beam and analyzed by a spectrometer (Andor Shamrock 193) coupled to a CCD camera (Andor iDus 401). A low-pass filter (Thorlabs FESH700) is placed in front of the spectrometer entrance to remove any unwanted light scattered from the fundamental beam.

2.4. Other characterization techniques.

Transmission Electron Microscopy (TEM), UV-visible absorption spectroscopy and Dynamic Light Scattering (DLS) working conditions are detailed in Supporting Information.

3. RESULTS

3.1. Structural characterization of LN@Au core-shell NPs

Core-shell LN@Au NPs were synthesized using a LbL process involving a first step of gold seeding onto BPEI-modified LN NPs followed by three gold reducing steps to grow and optimize the gold shell as already detailed.[25] TEM images of LN@Au NPs obtained after each reduction step are presented in **Figure 1a-c**. The gold shell has a raspberry shape composed of almost spherical gold NP drupelets with a diameter increasing after each reduction step. The measured diameters of the gold drupelets within the shell were 12.5 ± 2.5, 19.0 ± 4.1 and 26.0 ± 5.6 nm, after the first (R1), the second (R2) and the third (R3) reduction steps, respectively. These gold nanoparticles were attached to the 45 nm LN core thus increasing the diameter of LN@Au NPs after each growth step. After R3, the measured hydrodynamic diameter of LN@Au NPs was 163.3 ± 19.3 nm (which is consistent with their TEM diameter in **Figure 1c**) with a zeta potential value of 30.2 ± 2.8 mV,[25] showing their negligible aggregation level.

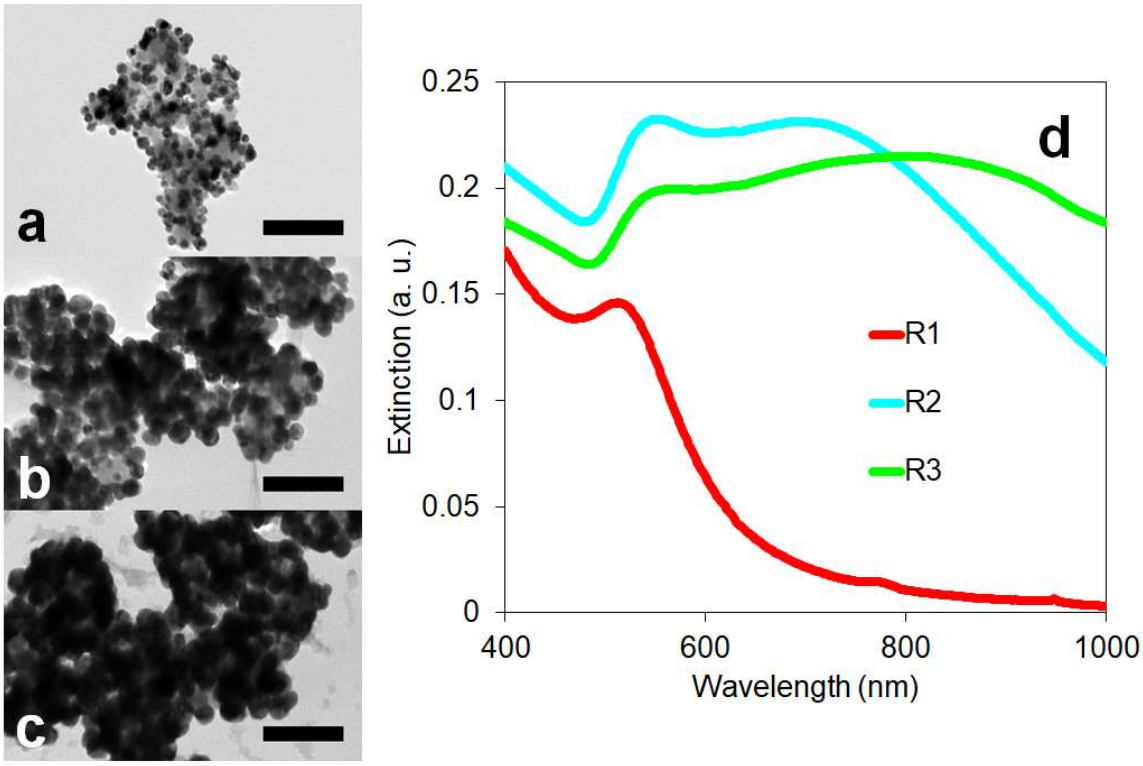

Figure 1. TEM images of LN@Au NPs with a constant 100 nm scale bar after (a) R1, (b) R2 and (c) R3 reduction steps and (d) corresponding extinction spectra (R1: red, R2: blue, R3: green).

An evolution of the UV-visible extinction spectra of LN@Au NPs is also clearly observed (**Figure 1d**) after each reduction. A single peak profile at 513 nm is obtained after R1, corresponding to non-interacting gold NPs at the surface of LN. After R2 and R3, this peak is shifted to 552 nm and 560 nm, respectively, and is still due to non-interacting gold NPs of larger size. Two broader extinction bands with a maximum at 698 nm for R2 and 803 nm for R3 are also visible showing that the plasmon band of LN@Au is progressively red-shifted during the gold shell growth. The red-shift of these broad bands as compared to the single peak obtained for R1 stems from the higher surface density of gold in the shell and the change of the environment electromagnetic properties. In addition, the presence of overlapping gold NPs results in plasmonic

coupling. If a slight red-shift may also be expected from the diameter increase of Au NPs, we demonstrate in the following section that this effect mainly arises from the gold surface coverage.

3.2. Modelling of the plasmon response of LN@Au core-shell NPs

DDA is a discrete solution method of the integral form of Maxwell's equations and has been shown to be well suited for predicting the optical response of nanostructures with complex geometries.[31] It was implemented here to study the plasmon response (**Figure 2**) of LN@Au hybrid NPs composed of a 45 nm LN core decorated with either 20 or 50 Au NPs of increasing diameter as derived from the TEM observations. In the numerical model, Au NPs and LN core were assumed as spheres. Au NPs were randomly generated on the LN core surface by using a Monte-Carlo process. The details of this generation method are given in Supporting Information. In the DDA, all NPs and core were discretized as set of dipoles organized in cubic arrangement of equal lattice spacing. The filling fraction was defined as the ratio of volume filled by gold to that of a complete imaginary shell of thickness equal to the NP size. This consists in calculating the ratio of the dipole number forming the NPs to that forming the imaginary full shell. It has to be noted here that this number of Au NPs per LN core is very low compared to the initial 1000:1 initial ratio which corresponds to the ratio of AuSeeds to LN NPs added in the reaction medium during the first step of the synthesis (seeding). The 20 to 50 Au NPs per LN core refers to the number of Au NPs finally attached to the LN core after the two synthesis steps (seeding and growth). Additionally, for these different geometries, the filling fraction defined by the ratio of the total volume of Au NPs to the volume of the corresponding full shell of same thickness,[31] was calculated (**Table 1**).

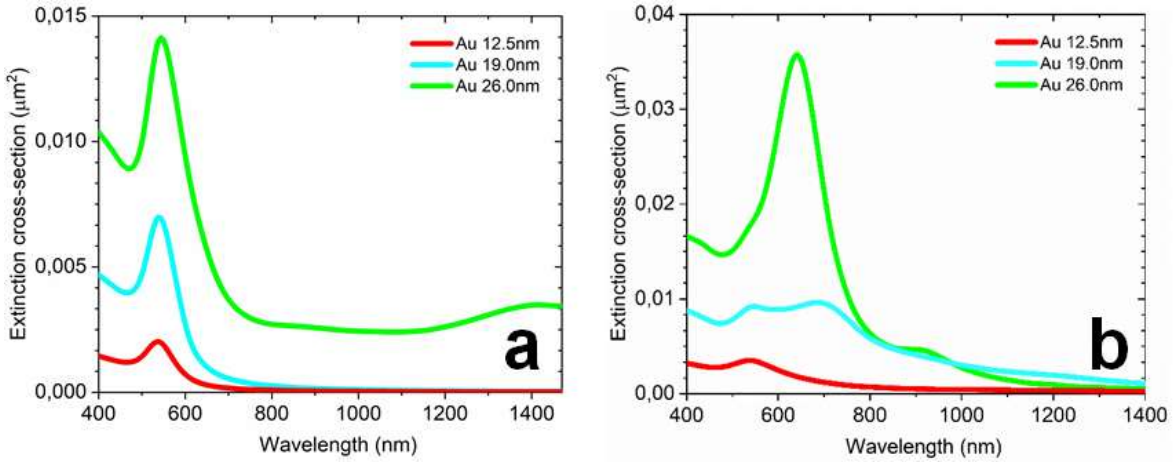

Figure 2. Calculated extinction cross-section spectra for core-shell NPs composed of a spherical 45 nm LN core decorated with (a) 20 and (b) 50 Au NPs of increasing diameter from 12.5 nm (R1), to 19 nm (R2) and to 26 nm (R3).

Table 1. Calculated filling fractions for 20 and 50 gold nanospheres of different diameters at the surface of a single 45 nm LN core.

Number of gold nanospheres per LN core	**Mean diameter of gold nanospheres**	**Filling fraction**
20	12.5	13.9%
20	19	25.7%
20	26	38.4%
50	12.5	37.2 %
50	19	61.2%
50	26	74.5%

A single plasmon peak was obtained for the lowest number of small Au NPs (**Figure 2a**) only showing a slight red-shift and peak broadening for the larger diameters. Note that the known plasmon response of individual, non-interacting Au nanospheres was retrieved with the diameters

fixed at 12.5 and 19 nm.[34] Concerning the larger Au NPs diameter of 26 nm, the extinction cross-section exhibits not only the usual plasmon peak of individual nanospheres with peak broadening but also a small second peak at long wavelength (1400 nm). After R3, it is not excluded that few close Au NPs touch each other or even slightly overlap and form isolated aggregates. The small peak at long wavelength is probably explained by the synergetic effect of plasmonic coupling between close Au NPs and an additional resonance mode of these few aggregates (**Figure S1, Supporting Information**).[31] When 50 Au NPs per LN core are considered, a double-peak plasmon band is already observed at R2 (Au NPs of 19 nm) with the first and second peak centered at 538 nm and 710 nm, respectively. After R3, a main peak is again derived at 640 nm (**Figure 2b**) corresponding to the nanoshell regime with the Au diameter at 26 nm. Gold NPs are then supposed to strongly overlap thus forming a quasi-continuous gold layer. It is worth noting that though the nanoshell regime is the dominant plasmon resonance regime after R3 with 50 Au NPs, another peak with moderate magnitude can be observed at around 920 nm wavelength and it indicates that the nanoshell is not entirely continuous. Interestingly, the characteristic two-peak response can be attributed to the black gold regime (broadband absorption) for which a weak overlap of the Au NPs results in aggregates of different sizes.[31] These two regimes actually depend on the filling fraction (**Table 1**). Assuming a single monolayer of randomly-distributed Au NPs and according to **Figure S2** (**Supporting Information**), the frontier between the two weakly interacting and strongly interacting regimes was found for a filling fraction around 47% when the average distance between adjacent Au NPs is null.[31] The filling fractions are all below 47% for 20 Au NPs per LN core consistently with the calculated plasmonic responses (**Figure 2a**) corresponding to non-interacting gold NPs. When the number of Au NPs is increased to 50, the double plasmon peak only observed in Figure 2b for the 19 nm diameter can be attributed to the weak overlapping regime

since the calculated filling fraction reaches 61% which is above the 47% frontier (**Figure S2, Supporting Information**). At 26 nm, the single peak observed is characteristic of the nanoshell regime while our experiments (Figure 1d) evidenced the double plasmon peak behaviour for both diameters measured at 19 nm and 26 nm after R2 and R3, respectively. This black gold regime is consistent though with the TEM image in Figure 1c where closely-packed Au NPs are observed but not a homogeneous shell. Such a difference between our experimental data and the modelling approach may indicate that the initial number of 50 Au NPs of diameter 26 nm per LN core is overestimated. Deriving the exact number (n) of individual Au NPs per LN core is indeed tricky from the TEM images so additional calculations were performed with n varying between 20 and 50 (Figure S3, Supporting Information). Computation results depicted in Figure 3a show that the extinction cross-section spectrum of LN@Au hybrid NPs varies with the number of NPs for a given core size. With n = 20 NPs decorating the LN, the extinction spectrum exhibits the single NP peak of plasmon resonance. This means that there is no noticeable plasmonic interaction between close NPs. This is expected since the filling fraction (38%) is below the theoretical limit of touching NPs (47%). Moreover, it can be evidenced from Figure 3a that NPs do not touch each other. As the number of NPs increases to 25, the single NP extinction peak broadens and at the same time, three moderate peaks took place at wavelengths of 750 nm, 900 nm and 1100 nm. In such a case, the filling fraction reaches 49.8 % from which some NPs are very close while others touch or overlap slightly their neighbours. Sufficiently close NPs interact via Coulomb interaction of opposite charges leading to the main peak broadening.[31] Touching or overlapping NPs behave as aggregates and exhibit new extinction peaks, responsible of the broadband extinction spectra. The positions of these peaks depend on the aggregate size and generally take place in the near infrared as evidenced here. Their moderate magnitudes are explained by the weak overlap of NPs

at the filling fraction of 49.8%. With 35 to 45 NPs, characterized by filling fractions of 62.8% to 66.7%, respectively, NPs overlap and start and start to form continuous NPs aggregates or quasi-complete nanoshell. The extinction spectrum exhibits strong near infrared plasmon resonance peak, known as nanoshell plasmonic regime. The interaction (or hybridization) of plasmons at the inner and outer interfaces of the shell controls the plasmon resonance peak. For LN@Au hybrid NPs with high filling fraction (typically greater than 60%), the shell thickness locally varies due to partial overlap of nanoparticles. Thus, strong and localized plasmon hybridization leads to broad plasmon peak. Increasing the number of NPs to 50, i.e. the filling fraction to 74%, leads to more uniform nanoshell thickness and decreases localized plasmon hybridization, which results to a blue shift of the plasmon peak along with an enhancement of the peak magnitude. The best comparison between the experimental (**Figure 1d**, green curve) and calculated (Figure 3a) extinction spectra is actually obtained for n = 39 for which the estimated filling fraction is 67%. A shouldering at 560 nm can indeed be noticed together with a large extinction band between 650 and 850 nm. Note that perfectly spherical cores and Au NPs are assumed in the modelling and that the experimental diameter and shape distributions of the LN cores and the gold NPs are not included in the calculations. For the wavelength corresponding to the extinction maximum ($\lambda_{max} = 676$ nm), the calculated extinction cross-section is $C_{ext\ max} = 0.0234$ μm^2, which is in agreement with the observed black gold regime.[31]

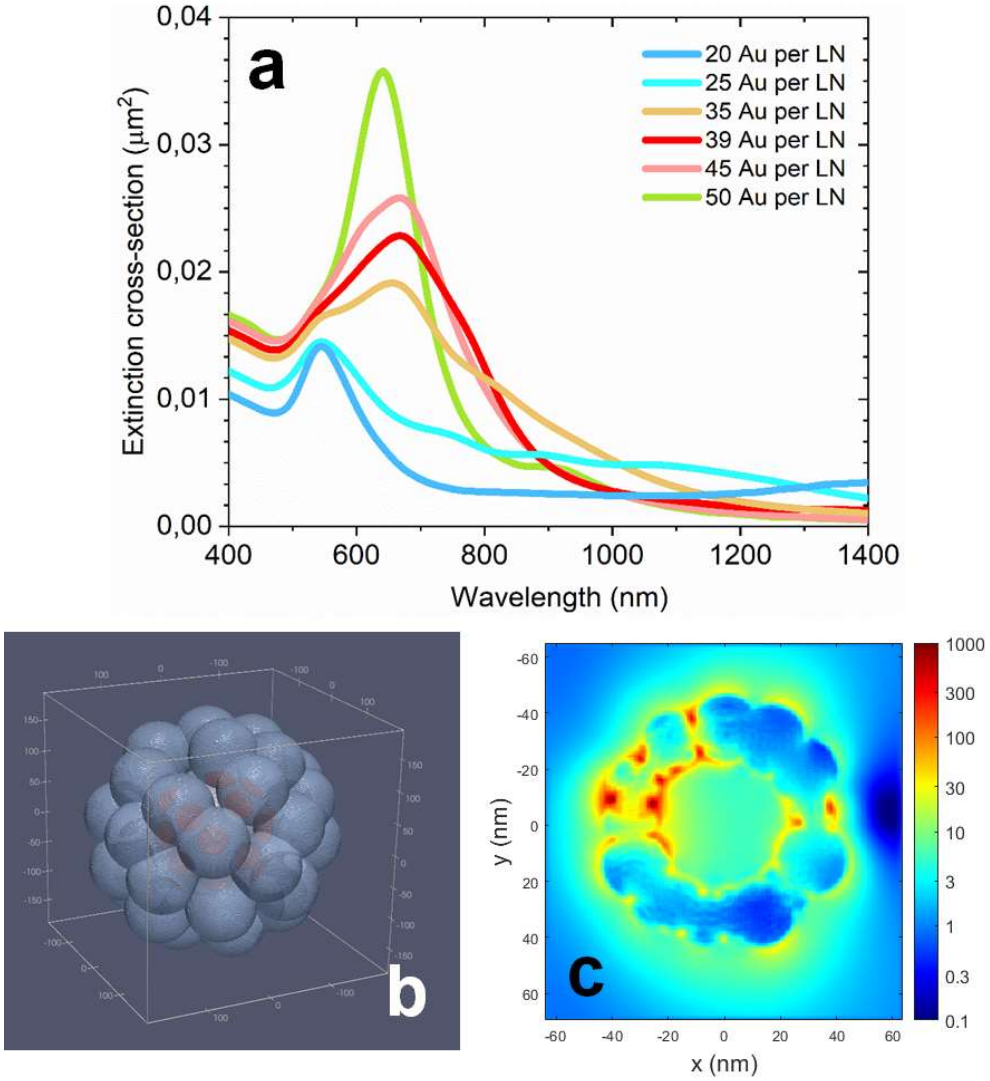

Figure 3. (a) Calculated extinction cross-section spectra for LN@Au NPs when the number of attached Au NPs of diameter 26 nm is increased from 20 to 50 at the surface of a single 45 nm LN core. (b) Dipole cubic array representation of a random distribution of 39 Au NPs of 26 nm diameter coating a LN core of 45 nm diameter with a filling fraction of 66.4%. Each voxel corresponds to a dipole lattice constant of 0.25 nm. (c) Corresponding cross-plane view of near-field enhancement $\frac{|E|^2}{|E_i|^2}$ at the wavelength 676 nm. E and E_i refer to the computed local and incident electric fields, respectively. The incident light wavevector is oriented along the X axis with the electric field direction oriented along Y.

For this optimized nanostructure configuration (n = 39 with 26 nm Au NPs diameter), the near-field enhancement due to the gold raspberry shell was calculated at the wavelength 676 nm, corresponding to the extinction maximum (Figures 3b and 3c). It showed that enhancement factors of the electric field reached values as high as 1000 in some local regions between overlapping gold NPs, due to the presence of electromagnetic 'hot spots'. The average $\frac{|E|^2}{|E_i|^2}$ enhancement factor integrated over the LN@Au system was evaluated to be 17.8.

3.3. Second Harmonic properties of LN@Au core-shell NPs

We performed a careful comparison of the SH signals from three different samples, namely LN@Au NPs (R3, three gold reducing steps), individual Au NPs (diameter 25 nm corresponding to a diameter similar to the one of gold NPs contained in the gold shell of LN@Au NPs after R3) and bare LN NPs. Hyper Rayleigh Scattering (HRS) technique was applied on colloidal suspensions to retrieve the hyperpolarizability value, the polarization response and the second harmonic spectral response of each type of NPs.

3.3.1. Magnitude of the First Hyperpolarizabilities

From a microscopic point view, measuring the first hyperpolarizability of the NPs is useful to quantitatively assess their SH cross-section and the impact of the gold shell on it. The internal method was used where the sample solution is diluted and the HRS intensity is collected and normalized to the neat solvent, here water. In this procedure, the background signal was always removed as it may arise from incoherent contributions. The latter procedure is also possible because the scattered light was collected over a short twenty nanometers spectral domain. As a result, the HRS intensity signal of each sample appeared as a Gaussian profile at half the fundamental wavelength sitting on a broadband background as shown in **Figure 4a** for LN@Au

NPs and in **Figures S4a and S5a** (**Supporting Information**), for Au NPs and bare LN cores, respectively. **Figure 4b** gives the linear plot of the HRS intensity normalized to the neat solvent intensity as a function of the LN@Au NPs concentration.

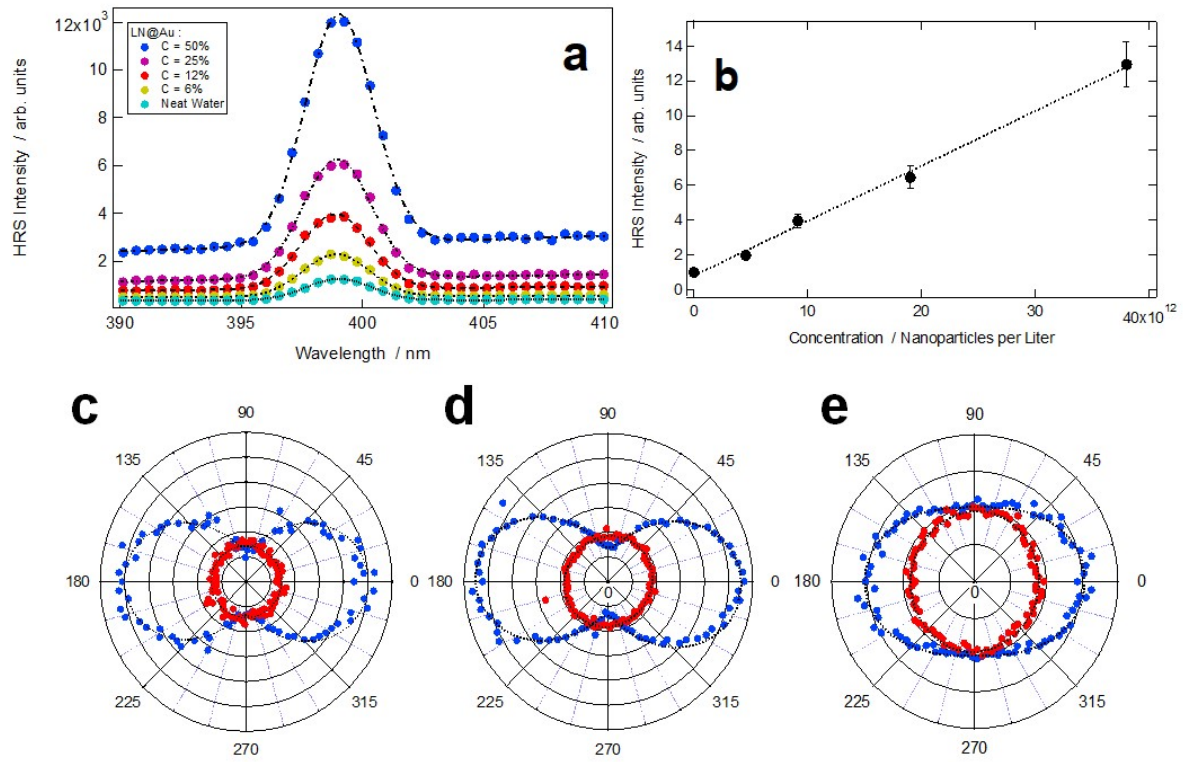

Figure 4. (a) HRS spectra of the LN@Au NPs for different concentrations of NPs, 100 % corresponding to 38 × 10^{12} NPs/L. (b) HRS intensities as a function of the LN@Au NPs concentration after normalization by that of the neat water solvent. (c-e) Polarization plots of the (blue) vertically polarized and (red) horizontally polarized HRS intensities as a function of the fundamental beam polarization angle for (c) LN NPs, (d) 25 nm diameter Au NPs and (e) LN@Au NPs.

The first hyperpolarizability of the NPs were obtained from the slope *b* of these line plots, given by **Eq. 1**:

$$b = \frac{\langle \beta_{NPs}^2 \rangle}{N_s \langle \beta_s^2 \rangle} \qquad \textbf{Eq. 1}$$

where β_{NPs} and β_s are the first hyperpolarizabilities of the NPs and neat solvent, respectively, and N_s the solvent concentration. The brackets indicate an orientational average since no preferential orientation occurs in the liquid suspension and the hyperpolarizability thus determined results from several microscopic nanoparticle tensor elements, following the standard procedure.[35] In determining β_{NPs} from the line plot slope, the reference values $\sqrt{\langle \beta_s^2 \rangle}$ = 0.087 × 10^{-30} esu and N_s = 55.5 M were used for neat water.[36] Experimental hyperpolarizabilities are reported in **Table 2**.

Table 2. First hyperpolarizability (in esu units) at 800 nm fundamental wavelength of the different NPs studied.

NPs	$\sqrt{\langle \boldsymbol{\beta}_{\boldsymbol{NPs}}^{\boldsymbol{2}} \rangle}$ **/esu**
LN	(0.77 +/- 0.03) ×10^{-24}
Au 25nm	(0.11 +/- 0.03) ×10^{-24}
LN@Au	(0.28 +/- 0.05) ×10^{-24}

The hyperpolarizability determined for the 25 nm diameter Au NPs is consistent with the one previously determined from gold NPs of similar diameter.[37] Interestingly, we point out in **Table 2** a weaker hyperpolarizability of the LN@Au NPs as compared to the LN cores. Contribution from the raspberry-like gold shell is thus detrimental to the overall hyperpolarizability of the hybrid NPs at a fundamental wavelength of 800 nm. The second harmonic scattering at 400 nm indeed falls in

the interband absorption region of gold NPs (**Figure S6, Supporting Information**). Despite the surface plasmon resonance of the attached gold NPs coating layer located at 800 nm (**Figure 1d**), it is suggested that absorption losses still hinder any resonance enhancement for the hybrid NPs. As a result, enhancement due to the shell should occurs at much longer excitation fundamental wavelengths for which losses are less predominant. Importantly, all experimental data were here monitored for diluted samples thus avoiding self-absorption of 2ω photons within the suspension.

3.3.2. Polarization-Resolved Measurements

In order to get further insights into the origin of the nonlinear response, polarization-resolved intensity plots, depicted in **Figures 4c, 4d and 4e**, were then recorded after rotating the input polarization angle γ and collecting the vertically- and horizontally-polarized HRS intensities with respect to the horizontal plane of scattering (**Figure S7, Supporting Information**). The plots were then adjusted according to **Eq. 2**.[37]

$$I_{HRS}^{\Gamma} = a^{\Gamma} cos^4\gamma + b^{\Gamma} cos^2\gamma sin^2\gamma + c^{\Gamma} sin^4\gamma \qquad \textbf{Eq. 2}$$

expressing the HRS intensity either vertically ($\Gamma = 0$) or horizontally polarized ($\Gamma = \pi/2$) as a function of the polarization angle γ of the fundamental beam. From the six intensity coefficients a^{Γ}, b^{Γ} and c^{Γ}, the depolarization ratio $D = c^0/a^0$ and the retardation parameters $\zeta^V = (b^0 - a^0 - c^0)/b^0$ and $\zeta^H = (a^{\pi/2} - c^{\pi/2})/(a^{\pi/2} + c^{\pi/2})$ were determined (see **Table 3**), thus providing a deeper analysis of the experimental nonlinear response. The D parameter provides a quantitative weight of the octupolar versus dipolar spherical tensors constituting the first hyperpolarizability tensor as obtained from an irreducible tensor decomposition. It thus determines

the dominant symmetry of the second-order nonlinear optical source. The two other parameters ζ^V and ζ^H provide information on the finite size of the nano-objects under study as they indicate the extent of the breaking of the point-like nanoparticle size approximation.

Table 3. Depolarization and retardation parameters D, ζ^V and ζ^H extracted from the polarization plots.

	$\boldsymbol{D}$	$\boldsymbol{\zeta^V}$	$\boldsymbol{\zeta^H}$
LN	0.16 ± 0.01	0.03 ± 0.01	-0.07 ± 0.01
Au 25nm	0.25 ± 0.01	0.05 ± 0.02	-0.03 ± 0.02
LN@Au	0.66 ± 0.02	-0.04 ± 0.01	0.04 ± 0.02

The derived depolarization ratio for the 25 nm diameter Au NPs is weaker than that previously reported but as it describes the origin of the HRS response, it strongly depends on the synthesis and relates to the surface geometry. Nevertheless, a value of 0.25 suggests a dipolar response within the irreducible tensor representation of the first hyperpolarizability whereas that of the LN@Au NPs is consistent with an octupolar response, namely a much more surface-distributed response.[38] This octupolar nature of the LN@Au NPs response is expected if the Au NPs shell contribution dominates over the LN core volume response or is largely non negligible. This observation is consistent though with the absolute magnitude of the first hyperpolarizability of these LN@Au NPs which is weaker than the one of pure LN NPs, see Table 2. The depolarization ratio of the pure LN NPs is also very different, with a dipolar value of D at 0.16.[24] The role of this raspberry-like gold shell is therefore clearly demonstrated.

Retardation effects appears very weak as seen from the close-to-zero values of the ζ^V and ζ^H parameters, as expected considering the NPs size, either pure Au NPs with a diameter of 25 nm

only, or pure LN cores at 45 nm and the core-shell NPs. Retardation parameters only deviate from zero for non-vanishing spatial phases, the latter being due to a non-negligible L/λ ratio where L is the nanoparticle size and λ the fundamental wavelength.

3.3.3. Second Harmonic Spectroscopy

After demonstrating the contribution of the black gold regime on the characteristic extinction spectra and lower hyperpolarizability value at 800 nm of the hybrid NPs comparatively to the bare LN core, Second Harmonic Spectroscopy (SHS) experiments[33] were conducted within the 700-1300 nm excitation range to get a better insight of the spectral response of each nanomaterial. First, the emission spectra of the different samples were measured for each excitation wavelength using a constant incident average power. Note that we only used diluted samples to limit absorption of the fundamental beam and re-absorption of the generated 2ω photons within the suspension. Moreover, the incident power was limited to 50 mW to prevent the occurrence of thermal lensing, which could induce self-defocusing of the fundamental beam, thereby modifying its intensity.[39] We addressed both of these concerns in the Supporting Information.

The image of the emission spectra as a function of the laser wavelength is shown in **Figure 5** for the LN@Au sample. For each spectrum, a SHG peak is superposed to a broad multiphoton luminescence background arising from the Au NPs[40] whereas for bare LN NPs only pure SHG is detected.

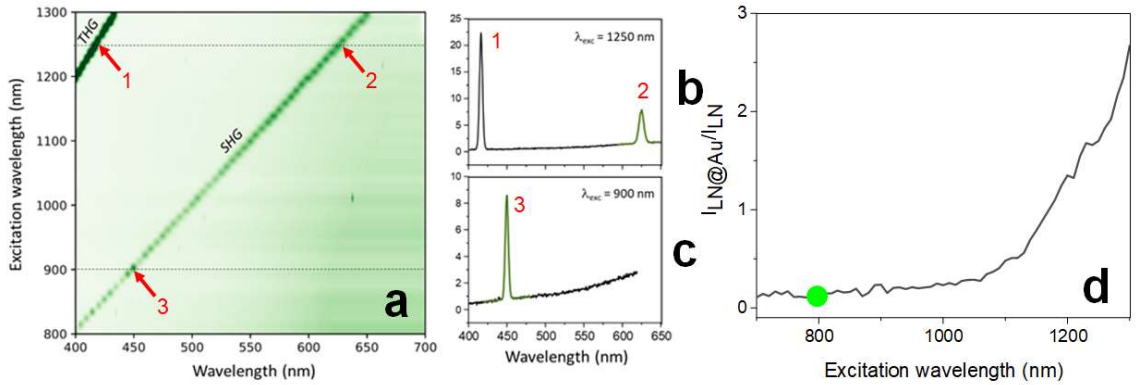

Figure 5. (a) Image of the emission spectra (x axis) as a function of the laser wavelength (y axis, 10-nm wavelength increments) for the LN@Au NPs suspension. Specific spectra at (b) 1250 nm excitation and (c) 900 nm excitation extracted from (a) showing SHG peaks at 625 nm (peak 2) and 450 nm (peak 3), respectively. Note that Third Harmonic Generation is also detected for laser wavelengths above 1200 nm (peak 1). (d) Normalized ratio of the SHS signal from LN@Au and LN suspensions as a function of the excitation wavelength. Normalization of the spectral response was made at λ = 800 nm according to the procedure described in the text (green circle).

SH intensities were retrieved for each excitation wavelength by fitting the SHG peak. We then calculated, as a function of the excitation wavelength, the experimental ratio $I_{LN@Au}/I_{LN}$ between the SH intensities from LN@Au and LN samples. The suspension of bare LN NPs, whose second-order susceptibility has a weak frequency-dispersion, is used here to correct the overall spectral response of the optical set-up in the 700-1300 nm excitation range.[33] Furthermore, it is worth noting that the experimental ratio, $I_{LN@Au}/I_{LN}$, is only relative because the concentration of LN suspension used here differs from that of LN@Au. We have thus normalized this relative spectral response by considering the hyperpolarizability values previously obtained and shown in **Table 2**. The absolute ratio $I_{LN@Au}/I_{LN}$ should be equal to the ratio of the squared hyperpolarizabilities

$\langle\beta^2_{LN@Au}\rangle/\langle\beta^2_{LN}\rangle = (0.28/0.77)^2 = 0.13$ at 800 nm if the same concentration is assumed for both samples. This corrected spectral response is shown in **Figure 5d** and reflects the enhancement or reduction of SHG associated with the formation of the raspberry-like gold shell. A significant increase of the scattered SH intensity by a factor up to ~20 can be observed between 800 and 1300 nm while a resonance above 1300 nm is expected but it was not completely resolved due to our limited excitation wavelength range.

Additionally, the SH spectral response of a colloidal suspension of bare Au NPs was also investigated using a similar experimental procedure (**Figure S9, Supporting Information**). Note that a very similar experimental response has been recently observed from 50 nm non-aggregated Au NPs using a comparable SHS experimental set-up.[40] For bare Au NPs, the SH intensity ratio shows a resonance of about ~ 10 at 1175 nm and is clearly different from the one found for the LN@Au sample. Interestingly, it can be concluded that the measured SH signal from LN@Au NPs cannot result from a simple addition of the individual contributions arising from the bare Au NPs and LN cores.

4. DISCUSSION

It is well known that linear and nonlinear spectral responses are closely correlated. SH enhancements are typically observed when the frequency ω of the incoming photons matches resonances in the linear spectrum at ω or 2ω. This has been demonstrated for many plasmonic[41] or hybrid nanostructures[14,42–44] and Mie dielectric nanoparticles[45,46] and can be explained by an increase of either the local field E_ω or the radiated harmonic far field $E_{2\omega}$. The following expression (**Eq. 3**) can be used to qualitatively interpret the SHG spectra response of any nanostructure:[19]

$$I_{2\omega} \propto \left(\int E_{loc}^2(\omega, \boldsymbol{r}) dV \right)^2 \left(\int E_{loc}^2(2\omega, \boldsymbol{r}) dV \right) \qquad \textbf{Eq. 3}$$

For the LN@Au sample, the plasmon band, whose origin was already discussed and attributed to the 'black gold regime', is broad and centered around 800 nm. Surprisingly, no equivalent band is observed in the nonlinear response excited at ω while the large SH intensity enhancement up to 1300 nm is compatible with a two-photon resonance at 1600 nm. Further near-field simulations were thus performed at 338 nm (half of the simulated extinction maximum) and 1352 nm (twice the simulated extinction maximum) but they do not show significant differences (F**igure S10, Supporting Information**) that could help to interpret the experimental response. The absence of any resonance at an excitation wavelength of 800 nm in the SHG response is still unclear but may be related to absorption losses as already suggested.[47,48] In addition, we can then question the exact origin of the measured SH properties of the LN@Au NPs. As already mentioned, SHG does not simply result from the addition of the signals generated by the LN and Au NPs separately, but to the formation of a raspberry-like gold shell. Typically, a strong SH signal can be induced by a favorable combination of the LN second-order nonlinear response and field enhancement due to a complete gold shell, as initially suggested by Pu *et al* for $BaTiO_3$/Au core-shell.[17] However, the SH properties can also mainly result from the gold nanostructure itself. For hybrid dielectric/metal structures, the exact source of nonlinearity is still questioned.[49] Recently, Faryad Ali *et al* demonstrated a 32-fold SHG signal enhancement for LN microspheres with Au NPs inserted into their mesoporous structure. Several hypotheses were proposed to explain the mechanism leading to enhanced SHG emission: coupling effects between Au NPs leading to an energy transfer back to the LN or superradiant plasmon scattering due to the collective interaction of Au NPs upon light excitation.[14] Noteworthy, a high SHG signal at 400 nm was also observed from NPs consisting of

a centrosymmetric 300 nm silica core surrounded by an incomplete gold shell[50] evidencing a rough surface similar to the raspberry-like morphology of the LN@Au NPs. The presence of plasmonic 'hot spots' leading to very large field factor enhancement then results in these high SHG signals from the gold surface. In another recent study, a SHG signal increase of about 10^4 has been measured after the aggregation of individual gold NPs with an expected resonance beyond 1300 nm.[40] Interestingly, their SHG spectral response is very close to our current measurements. Moreover, polarization-resolved measurements at 800 nm strongly support here a dominant surface contribution compared to the core volume response of LN while DDA simulation for plasmonic vesicles[31] demonstrated that near-field electrical field enhancement is mainly localized between the Au NPs shell when considering the 'black gold regime' (**Figure 3c**).[31] We can therefore assume that the morphology of the raspberry-like gold shell with a random distribution of the Au NPs attached to the LN core is here at the origin of the experimentally-derived SHG properties.

5. CONCLUSION

This paper aims to investigate both the plasmonic and the second harmonic emission properties of hybrid lithium niobate-gold nanoparticles with a raspberry-like gold shell structure grown onto LN cores after three successive gold reduction steps. Their structural characterizations evidenced an increase of the Au NPs diameter from 12.5 to 26.0 nm, associated with a progressive red-shift of the plasmon band. This plasmonic response was modelled using DDA method. Several plasmonic regimes were identified depending on the filling fraction related to the gold surface coverage. An average number of 39 gold nanoparticles per lithium niobate core, corresponding to a filling fraction of 67%, was found to be the best model explaining the experimental plasmonic

response of the final hybrid nanostructures. This response was attributed to the black gold regime resulting in a high extinction cross-section and electromagnetic 'hot spots' in the region between overlapping gold nanoparticles. Second harmonic properties of bare LN cores and Au NPs of diameter 25 nm, and of hybrid LN@Au nanostructures were then studied and quantitatively assessed. HRS measurements were performed by using two complementary techniques in order to investigate the hyperpolarizability values, polarization response and second harmonic spectral response of each type of nanoparticles. At an excitation wavelength of 800 nm, the weaker hyperpolarizability value measured for the LN@Au NPs, comparatively to the LN cores, was measured together with an octupolar polarization response. Moreover, shifting the excitation at 1300 nm leads to a up to 20-fold increase of the SH intensity. Origin of the nonlinear response was attributed to dominant surface contributions in the hybrid nanostructures due to the black gold regime associated to the as-prepared raspberry-like gold shell.

ASSOCIATED CONTENT

Supporting Information. Detailed protocol for lithium niobate-gold (LN@Au) core-shell NPs synthesis, characterization techniques, computed near-field enhancement of the 26 nm LN coated with 20 NPs at 1400 nm wavelength, relationship between the nanoshell filling fraction and the average distance between adjacent Au NP surfaces, dipole cubic array representation of random distributions of different number of Au NPs (26 nm diameter) coating a LN core (45 nm diameter), HRS spectra of Au and LN NPs for different concentrations, HRS intensities as a function of NPs concentration after normalization by the response of neat water, extinction spectrum of 25 nm gold nanoparticles, illustration of the polarization-resolved experimental set-up for the Hyper Rayleigh Scattering measurements and the determination of the first

hyperpolarizabilities, ratio of the SHS signal from Au and LN NPs suspensions as a function of the excitation wavelength, computed near-field enhancement of the 26 nm LN coated with 39 NPs at 338 nm and 1352 nm wavelengths. The following files are available free of charge.

AUTHOR INFORMATION

Corresponding Author

*Virginie Monnier (virginie.monnier@ec-lyon.fr)

Author Contributions

K. B., Z. B., R. T. and M. U. carried out the experiments. V. M. wrote the manuscript with support from Y. M., R. L. D., J. H. R. and P.-F. B. Correction and review were performed by all authors. All authors have given approval to the final version of the manuscript.

Funding Sources

This work was supported by ANR in the frame of RACINE project (ANR-17-CE24-0029-03) and the 2015-2020 French Contrat Plan Etat Région (project E-TIME, SYMME).

ACKNOWLEDGMENT

This work was supported by ANR in the frame of RACINE project (ANR-17-CE24-0029-03) and the 2015-2020 French Contrat Plan Etat Région (project E-TIME, SYMME). N. Blanchard from CLYM platform is thanked for his help with TEM experiments.

ABBREVIATIONS

LN, lithium niobate; NPs, nanoparticles; HRS, Hyper Rayleigh Scattering; DDA, Discrete-Dipole Approximation; SH, Second Harmonic.

REFERENCES

(1) Shiigi, H.; Yamamoto, Y.; Yoshi, N.; Nakao, H.; Nagaoka, T. One-Step Preparation of Positively-Charged Gold Nanoraspberry. *Chem. Commun.* **2006**, *30* (41), 4288–4290. https://doi.org/10.1039/b610085f.

(2) Gandra, N.; Portz, C.; Nergiz, S. Z.; Fales, A.; Vo-Dinh, T.; Singamaneni, S. Inherently Stealthy and Highly Tumor-Selective Gold Nanoraspberries for Photothermal Cancer Therapy. *Sci. Rep.* **2015**, *5* (May), 10311. https://doi.org/10.1038/srep10311.

(3) Cheng, Y.; Ding, Y.; Chen, J.; Xu, W.; Wang, W.; Xu, S. Au Nanoparticles Decorated Covalent Organic Framework Composite for SERS Analyses of Malachite Green and Thiram Residues in Foods. *Spectrochim. Acta Part A Mol. Biomol. Spectrosc.* **2022**, *281* (July), 121644.

(4) Plan Sangnier, A.; Van de Walle, A.; Aufaure, R.; Fradet, M.; Motte, L.; Guénin, E.; Lalatonne, Y.; Wilhelm, C. Endosomal Confinement of Gold Nanospheres, Nanorods, and Nanoraspberries Governs Their Photothermal Identity and Is Beneficial for Cancer Cell Therapy. *Adv. Biosyst.* **2020**, *4* (4), 1900284. https://doi.org/10.1002/adbi.201900284.

(5) Dikmen, Z.; Javanifar, R.; Bütün, V. Fluorescent Poly(Methacryloxy Quinolin) Microparticles Allowing Simultaneous Gold Detection with Additive-Free Photocatalytic Synthesis of Raspberry-like Gold Nanoparticles and Gold Nanoparticle Decorated Microparticles. *Eur. Polym. J.* **2020**, *129* (February), 109623. https://doi.org/10.1016/j.eurpolymj.2020.109623.

(6) Le Beulze, A.; Gomez-Graña, S.; Gehan, H.; Mornet, S.; Ravaine, S.; Correa-Duarte, M.; Guerrini, L.; Alvarez-Puebla, R. A.; Duguet, E.; Pertreux, E. et al. Robust Raspberry-like Metallo-Dielectric Nanoclusters of Critical Sizes as SERS Substrates. *Nanoscale* **2017**, *9* (17), 5725–5736. https://doi.org/10.1039/c7nr00969k.

(7) Höller, R. P. M.; Dulle, M.; Thomä, S.; Mayer, M.; Steiner, A. M.; Förster, S.; Fery, A.; Kuttner, C.; Chanana, M. Protein-Assisted Assembly of Modular 3D Plasmonic Raspberry-like Core/Satellite Nanoclusters: Correlation of Structure and Optical Properties. *ACS Nano* **2016**, *10* (6), 5740–5750. https://doi.org/10.1021/acsnano.5b07533.

(8) Keyvan Rad, J.; Alinejad, Z.; Khoei, S.; Mahdavian, A. R. Controlled Release and Photothermal Behavior of Multipurpose Nanocomposite Particles Containing Encapsulated Gold-Decorated Magnetite and 5-FU in Poly(Lactide-Co-Glycolide). *ACS Biomater. Sci. Eng.* **2019**, *5* (9), 4425–4434. https://doi.org/10.1021/acsbiomaterials.9b00790.

(9) Smirnov, E.; Peljo, P.; Girault, H. H. Gold Raspberry-Like Colloidosomes Prepared at the Water-Nitromethane Interface. *Langmuir* **2018**, *34* (8), 2758–2763. https://doi.org/10.1021/acs.langmuir.7b03532.

(10) Wu, Y.; Liu, Y.; Tang, X.; Cheng, Z.; Liu, H. Tunable Plasmonics of Hollow Raspberry-like Nanogold for the Robust Raman Scattering Detection of Antibiotics on a Portable Raman Spectrometer. *Analyst* **2020**, *145* (17), 5854–5860. https://doi.org/10.1039/d0an01049a.

(11) Vuilleumier, J.; Gaulier, G.; De Matos, R.; Mugnier, Y.; Campargue, G.; Wolf, J.-P.; Bonacina, L.; Gerber-Lemaire, S. Photocontrolled Release of the Anticancer Drug Chlorambucil with Caged Harmonic Nanoparticles. *Helv. Chim. Acta* **2019**, *103*, e1900251.

https://doi.org/10.1002/hlca.201900251.

(12) Campargue, G.; La Volpe, L.; Giardina, G.; Gaulier, G.; Lucarini, F.; Gautschi, I.; Le Dantec, R.; Staedler, D.; Diviani, D.; Mugnier, Y. et al. Multiorder Nonlinear Mixing in Metal Oxide Nanoparticles. *Nano Lett.* **2020**, *20* (12), 8725–8732. https://doi.org/10.1021/acs.nanolett.0c03559.

(13) De Matos, R.; Gheata, A.; Campargue, G.; Vuilleumier, J.; Nicolle, L.; Pierzchala, K.; Jelescu, I.; Lucarini, F.; Gautschi, I.; Riporto, F. et al. Gd3+-Functionalized Lithium Niobate Nanoparticles for Dual Multiphoton and Magnetic Resonance Bioimaging. *ACS Appl. Nano Mater.* **2022**, *5*, 2912–2922.

(14) Faryad Ali, R.; Busche, J. A.; Kamal, S.; Masiello, D. J.; Gates, B. D. Near-Field Enhancement of Optical Second Harmonic Generation in Hybrid Gold–Lithium Niobate Nanostructures. *Light Sci. Appl.* **2023**, *12* (1), 99. https://doi.org/10.1038/s41377-023-01092-8.

(15) Gürdal, E.; Horneber, A.; Shaqqura, N.; Meixner, A. J.; Kern, D. P.; Zhang, D.; Fleischer, M. Enhancement of the Second Harmonic Signal of Nonlinear Crystals by Self-Assembled Gold Nanoparticles. *J. Chem. Phys.* **2020**, *152* (10), 104711. https://doi.org/10.1063/1.5139893.

(16) Gürdal, E.; Horneber, A.; Meixner, A. J.; Kern, D. P.; Zhang, D.; Fleischer, M. Enhancement of the Second Harmonic Signal of Nonlinear Crystals by a Single Metal Nanoantenna. *Nanoscale* **2020**, *12* (45), 23105–23115. https://doi.org/10.1039/d0nr05696k.

(17) Pu, Y.; Grange, R.; Hsieh, C. L.; Psaltis, D. Nonlinear Optical Properties of Core-Shell

Nanocavities for Enhanced Second-Harmonic Generation. *Phys. Rev. Lett.* **2010**, *104* (20), 207402. https://doi.org/10.1103/PhysRevLett.104.207402.

(18) Zhang, Y.; Manjavacas, A.; Hogan, N. J.; Zhou, L.; Ayala-Orozco, C.; Dong, L.; Day, J. K.; Nordlander, P.; Halas, N. J. Toward Surface Plasmon-Enhanced Optical Parametric Amplification (SPOPA) with Engineered Nanoparticles: A Nanoscale Tunable Infrared Source. *Nano Lett.* **2016**, *16* (5), 3373–3378. https://doi.org/10.1021/acs.nanolett.6b01095.

(19) Madzharova, F.; Nodar, Á.; Živanović, V.; Huang, M. R. S.; Koch, C. T.; Esteban, R.; Aizpurua, J.; Kneipp, J. Gold- and Silver-Coated Barium Titanate Nanocomposites as Probes for Two-Photon Multimodal Microspectroscopy. *Adv. Funct. Mater.* **2019**, *29* (49), 1–13. https://doi.org/10.1002/adfm.201904289.

(20) Shi, J.; Li, Y.; Kang, M.; He, X.; Halas, N. J.; Nordlander, P.; Zhang, S.; Xu, H. Efficient Second Harmonic Generation in a Hybrid Plasmonic Waveguide by Mode Interactions. *Nano Lett.* **2019**, *19* (6), 3838–3845. https://doi.org/10.1021/acs.nanolett.9b01004.

(21) Ai, Q.; Sterl, F.; Zhang, H.; Wang, J.; Giessen, H. Giant Second Harmonic Generation Enhancement in a High-Q Doubly Resonant Hybrid Plasmon–Fiber Cavity System. *ACS Nano* **2021**, *15*, 19409–19417.

(22) Daoudi, C.; Metidji, M. O.; Remram, M.; Jurdyc, A.-M.; Martini, M.; Gehan, H.; Vouagner, D. Nano-Assembling and Optical Properties of Sub-100 Nm Raspberry-like Nanoparticles. *Eur. Phys. J. Appl. Phys.* **2018**, *82*, 20401.

(23) Yi, J. M.; Wang, D.; Schwarz, F.; Zhong, J.; Chimeh, A.; Korte, A.; Zhan, J.; Schaaf, P.; Runge, E.; Lienau, C. Doubly Resonant Plasmonic Hot Spot-Exciton Coupling Enhances

Second Harmonic Generation from Au/ZnO Hybrid Porous Nanosponges. *ACS Photonics* **2019**, *6* (11), 2779–2787. https://doi.org/10.1021/acsphotonics.9b00791.

(24) Taitt, R.; Urbain, M.; Behel, Z.; Pablo-Sainz-Ezquerra, A.-M.; Kandybka, I.; Millet, E.; Martinez-Rodriguez, N.; Yeromonahos, C.; Beauquis, S.; Le Dantec, R. et al. Gold-Seeded Lithium Niobate Nanoparticles : Influence of Gold Surface Coverage on Second Harmonic Properties. *Nanomaterials* **2021**, *11*, 950. https://doi.org/10.3390/nano11040950.

(25) Taitt, R.; Urbain, M.; Bredillet, K.; Behel, Z.; Ceccone, G.; Bañuls-Ciscar, J.; Beauquis, S.; Mugnier, Y.; Brevet, P. F.; Le Dantec, R. et al. Gold Raspberry Shell Grown onto Nonspherical Lithium Niobate Nanoparticles for Second Harmonic Generation and Photothermal Applications. *Part. Part. Syst. Charact.* **2022**, 2200093. https://doi.org/10.1002/ppsc.202200093.

(26) Urbain, M.; Riporto, F.; Beauquis, S.; Monnier, V.; Marty, J. C.; Galez, C.; Durand, C.; Chevolot, Y.; Le Dantec, R.; Mugnier, Y. On the Reaction Pathways and Growth Mechanisms of LiNbO3 Nanocrystals from the Non-Aqueous Solvothermal Alkoxide Route. *Nanomaterials* **2021**, *11* (1), 154. https://doi.org/10.3390/nano11010154.

(27) Dantelle, G.; Beauquis, S.; Le Dantec, R.; Monnier, V.; Galez, C.; Mugnier, Y. Solution-Based Synthesis Routes for the Preparation of Noncentrosymmetric 0-D Oxide Nanocrystals with Perovskite and Nonperovskite Structures. *Small* **2022**, *18*, 2200992. https://doi.org/10.1002/smll.202200992.

(28) Duff, D. G.; Baiker, A.; Edwards, P. P. A New Hydrosol of Gold Clusters. 1. Formation and Particle Size Variation. *Langmuir* **1993**, *9*, 2301–2309. https://doi.org/10.1039/c39930000096.

(29) Draine, B. T.; Flatau, P. J. Discrete-Dipole Approximation for Scattering Calculations. *J. Opt. Soc. Am. A* **1994**, *11* (4), 1491–1499.

(30) Zelmon, D. E.; Small, D. L. Infrared Corrected Sellmeier Coefficients for Congruently Grown Lithium Niobate and 5 Mol. % Magnesium Oxide-Doped Lithium Niobate. *J. Opt. Soc. Am. B* **1997**, *14* (12), 3319–3322.

(31) Randrianalisoa, J.; Li, X.; Serre, M.; Qin, Z. Understanding the Collective Optical Properties of Complex Plasmonic Vesicles. *Adv. Opt. Mater.* **2017**, *5* (20), 1–11. https://doi.org/10.1002/adom.201700403.

(32) Russier-Antoine, I.; Lee, H. J.; Wark, A. W.; Butet, J.; Benichou, E.; Jonin, C.; Martin, O. J. F.; Brevet, P. F. Second Harmonic Scattering from Silver Nanocubes. *J. Phys. Chem. C* **2018**, *122* (30), 17447–17455. https://doi.org/10.1021/acs.jpcc.8b04299.

(33) Riporto, J.; Urbain, M.; Mugnier, Y.; Multian, V.; Riporto, F.; Bredillet, K.; Beauquis, S.; Galez, C.; Monnier, V.; Chevolot, Y. et al. Second Harmonic Spectroscopy of ZnO, BiFeO3 and LiNbO3 Nanocrystals. *Opt. Mater. Express* **2019**, *9* (4), 1955–1966. https://doi.org/10.1364/OME.9.001955.

(34) Link, S.; El-Sayed, M. A. Size and Temperature Dependence of the Plasmon Absorption of Colloidal Gold Nanoparticles. *J. Phys. Chem. B* **1999**, *103*, 4212–4217.

(35) Bersohn, R.; Pao, Y.-H.; Frisch, H. L. Double - Quantum Light Scattering by Molecules. *J. Chem. Phys* **1966**, *45*, 3184–3198.

(36) Duboisset, J.; Matar, G.; Russier-Antoine, I.; Benichou, E.; Bachelier, G.; Jonin, C.; Ficheux, D.; Besson, F.; Brevet, P. F. First Hyperpolarizability of the Natural Aromatic

Amino Acids Tryptophan, Tyrosine, and Phenylalanine and the Tripeptide Lysine-Tryptophan-Lysine Determined by Hyper-Rayleigh Scattering. *J. Phys. Chem. B* **2010**, *114* (43), 13861–13865. https://doi.org/10.1021/jp105554s.

(37) Russier-Antoine, I.; Benichou, E.; Bachelier, G.; Jonin, C.; Brevet, P. F. Multipolar Contributions of the Second Harmonic Generation from Silver and Gold Nanoparticles. *J. Phys. Chem. C* **2007**, *111* (26), 9044–9048. https://doi.org/10.1021/jp0675025.

(38) Brasselet, S.; Zyss, J. Multipolar Molecules and Multipolar Fields: Probing and Controlling the Tensorial Nature of Nonlinear Molecular Media. *J. Opt. Soc. Am. B* **1998**, *15* (1), 257–288. https://doi.org/10.1364/josab.15.000257.

(39) Bredillet, K.; Riporto, J.; Forcherio, G. T.; Dunklin, J. R.; Wolf, J. P.; Bonacina, L.; Mugnier, Y.; Le Dantec, R. Dispersion of the Nonlinear Susceptibility of MoS2 and WS2 from Second-Harmonic Scattering Spectroscopy. *Phys. Rev. B* **2020**, *102* (23), 235408. https://doi.org/10.1103/PhysRevB.102.235408.

(40) de Coene, Y.; Deschaume, O.; Zhang, Y.; Billen, A.; He, J.; Seré, S.; Knoppe, S.; Van Cleuvenbergen, S.; Verbiest, T.; Clays, K. et al. Enhancement of Nonlinear Optical Scattering by Gold Nanoparticles through Aggregation-Induced Plasmon Coupling in the Near-Infrared. *ChemPhysChem* **2019**, *20* (13), 1765–1774. https://doi.org/10.1002/cphc.201900194.

(41) Metzger, B.; Hentschel, M.; Giessen, H. Ultrafast Nonlinear Plasmonic Spectroscopy: From Dipole Nanoantennas to Complex Hybrid Plasmonic Structures. *ACS Photonics* **2016**, *3* (8), 1336–1350. https://doi.org/10.1021/acsphotonics.5b00587.

(42) Aouani, H.; Rahmani, M.; Navarro-Cía, M.; Maier, S. A. Third-Harmonic-Upconversion Enhancement from a Single Semiconductor Nanoparticle Coupled to a Plasmonic Antenna. *Nat. Nanotechnol.* **2014**, *9* (4), 290–294. https://doi.org/10.1038/nnano.2014.27.

(43) Hentschel, M.; Metzger, B.; Knabe, B.; Buse, K.; Giessen, H. Linear and Nonlinear Optical Properties of Hybrid Metallic-Dielectric Plasmonic Nanoantennas. *Beilstein J. Nanotechnol.* **2016**, *7* (1), 111–120. https://doi.org/10.3762/bjnano.7.13.

(44) Linnenbank, H.; Grynko, Y.; Förstner, J.; Linden, S. Second Harmonic Generation Spectroscopy on Hybrid Plasmonic/Dielectric Nanoantennas. *Light Sci. Appl.* **2016**, *5* (1), e16013–e16013. https://doi.org/10.1038/lsa.2016.13.

(45) Gili, V. F.; Carletti, L.; Locatelli, A.; Rocco, D.; Finazzi, M.; Ghirardini, L.; Favero, I.; Gomez, C.; Lemaître, A.; Celebrano, M. et al. Monolithic AlGaAs Second-Harmonic Nanoantennas: Erratum. *Opt. Express* **2016**, *24*, 15965–15971. https://doi.org/10.1364/oe.425110.

(46) Timpu, F.; Sendra, J.; Renaut, C.; Lang, L.; Timofeeva, M.; Buscaglia, M. T.; Buscaglia, V.; Grange, R. Lithium Niobate Nanocubes as Linear and Nonlinear Ultraviolet Mie Resonators. *ACS Photonics* **2019**, *6* (2), 545–552. https://doi.org/10.1021/acsphotonics.8b01594.

(47) Butet, J.; Brevet, P.-F.; Martin, O. J. F. Optical Second Harmonic Generation in Plasmonic Nanostructures: From Fundamental Principles to Advanced Applications. *ACS Nano* **2015**, *9* (11), 10545–10562. https://doi.org/10.1021/acsnano.5b04373.

(48) Zhu, M.; Abdollahramezani, S.; Li, C.; Fan, T.; Harutyunyan, H.; Adibi, A. Dynamically

Tunable Harmonic Generation Using Hybrid Metasurfaces Incorporating Phase-Change Chalcogenides. *Nanophotonics* **2022**, *11* (11), 2727–2735. https://doi.org/10.1364/cleo_si.2022.sf2n.7.

(49) Chauvet, N.; Ethis De Corny, M.; Jeannin, M.; Laurent, G.; Huant, S.; Gacoin, T.; Dantelle, G.; Nogues, G.; Bachelier, G. Hybrid KTP-Plasmonic Nanostructures for Enhanced Nonlinear Optics at the Nanoscale. *ACS Photonics* **2020**, *7* (3), 665–672. https://doi.org/10.1021/acsphotonics.9b01484.

(50) Sauerbeck, C.; Haderlein, M.; Schürer, B.; Braunschweig, B.; Peukert, W.; Klupp Taylor, R. N. Shedding Light on the Growth of Gold Nanoshells. *ACS Nano* **2014**, *8* (3), 3088–3096. https://doi.org/10.1021/nn500729r.

TOC Graphic.

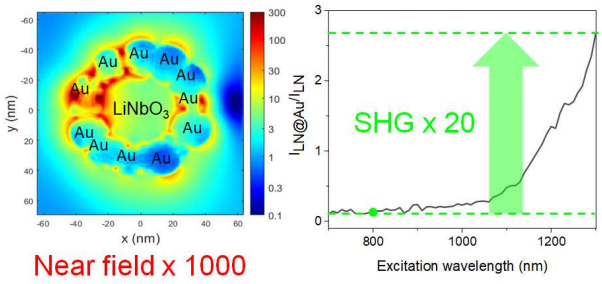
Au
LiNbO3
y (nm)
x (nm)
300
100
30
10
3
1
0.3
0.1
I_LN@Au/I_LN
SHG x 20
Excitation wavelength (nm)
Near field x 1000